

PREDICTING ENERGY DISSIPATION CHARACTERISTICS OF A TUMBLING GRANULAR-FLOW DAMPER USING DEM

Sergiu DRAGOMIR^{1,2*} Matthew SINNOTT², Eren SEMERCIGIL¹ and Ozden TURAN¹

¹ School of Engineering and Science, Faculty of Health, Engineering and Science, Victoria University

² CSIRO Mathematics and Information Sciences, Clayton, Victoria 3169, AUSTRALIA

*Corresponding author, E-mail address: sergiu.dragomir@csiro.au

ABSTRACT

Although the effectiveness of granular dissipation has been demonstrated through experimental observations, the development of a numerical model would provide a valuable design tool to study the relevant mechanics in detail and to construct meaningful non-dimensional parameters for scale-up. The objective of this paper is to report the results of modelling a tumbling granular dissipater using the Discrete Element Method (DEM) technique. Analysis of the granular flow is performed with a focus on highly energetic and dissipative events. These events are investigated to determine the nature of the dissipation in this system, the mechanisms responsible, and how dissipation levels can be controlled for the purpose of developing a tuned absorber.

NOMENCLATURE

k spring stiffness
 μ coefficient of friction
 e coefficient of restitution
 C damping coefficient
 x particle overlap
 v speed
 $a/b, b/c$ super-quadric particle aspect ratio
 n super-quadric particle blockiness

INTRODUCTION

Tall and flexible structures require protection from dynamic loads, such as those resulting from strong winds or earthquakes, as a matter of both safety and comfort. A variety of tuned vibration absorbers can be used to attenuate excessive oscillations of these structures. Such devices consist of a mechanism to transfer energy away from the structure (ensured by a tuning process) and dissipative elements. A rolling/tumbling container partially filled with a granular material, has been observed to be an effective energy dissipater (Dragomir et al. 2007). Tumbling granular assemblies hold significant promise for enhancing the effectiveness of tuned absorbers for structural control.

Particle-based numerical models are well suited to model granular flows since they are able to represent each individual contact interaction. The Discrete Element Method (DEM) is a particle-based method which tracks the motion of individual particles and it has been reviewed by Campbell (2006), Barker (1994) and Walton (1992). A DEM granular solver developed by CSIRO is used here.

The CSIRO solver has been successfully applied to a wide range of applications from mining to pharmaceuticals by Cleary (1998, 2001, 2008) and Sinnott et al. (2006).

This work is the numerical verification of the experimental setup presented by Dragomir et al. (2009). A brief description of the numerical method is given next. Then, numerical predictions and comparisons to experiment are discussed.

Discrete Element Method

The DEM solver uses a linear spring-dashpot contact model and is described in more detail by Sinnott et al. (2006). Figure 1 is a simple schematic of the mechanical model. In the normal direction to the contact, the force F_n is

$$F_n = -k_n \Delta x + C_n v_n \quad (1)$$

where k_n and C_n are the contact stiffness and damping coefficients respectively, Δx is the amount of overlap, and v_n is the normal speed. The first term (the spring) in (1) represents the resistance to deformation, whereas the second term (the dashpot) is the equivalent viscous damping force, proportional to the normal speed. The spring is a purely repulsive force, to avoid non-physical attractive forces. The amount of overlap is determined by k_n .

The desired average overlap for the system should be less than 0.5% of the particle size. The damping coefficient C_n is dictated by the coefficient of restitution e . In the tangential direction, the contact force F_t is expressed as

$$F_t = \min(\mu F_n, k_t \int v_t dt + c_t v_t) \quad (2)$$

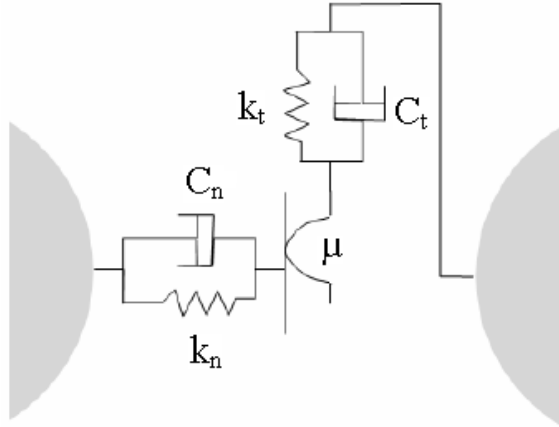


Figure 1: Schematic representation of DEM model

where μ is the friction coefficient, k_t and C_t are stiffness and damping coefficients respectively, and v_t is the speed in the tangential (shear) direction. The integral term represents the elastic deformation in the tangential direction. The total force is limited by the Coulomb force (μF_t). When it is reached, sliding of the contact surfaces begins.

The boundary of any object interacting with particles can be represented as a triangular mesh. Particles can overlap individual mesh element surfaces and define normal and tangential contact forces using the same linear spring-dashpot model as (1) and (2).

Super-quadric shapes are used to model the particles as opposed to more commonly used spheres, as spheres cannot predict the shear resistance and dilation of particle beds accurately (Cleary 2008, Cleary et al. 2008). The most general form of super-quadrics is:

$$\left(\frac{x}{a}\right)^n + \left(\frac{y}{b}\right)^n + \left(\frac{z}{c}\right)^n = 1 \quad (3)$$

The fractions b/a and c/a are the aspect ratios in the xy and xz directions respectively. For $a = b = c$ and $n = 2$, the resulting particle is a sphere. As n increases, the particle shape approaches that of a cube with progressively sharper corners.

The typical DEM algorithm tracks all particles and collisions within the system being modelled and collects the resulting forces on the particles and on the boundaries, so as to sufficiently resolve the contact dynamics. Several statistics relevant to energy dissipation are recorded for the purposes of investigating flow related mechanisms responsible for dissipation in the rolling container.

The particles used have size and shape parameters which are representative of sand particles as in the experiments. The particles are super-quadrics with blockiness parameter

n randomly distributed with a uniform probability between 2.5 and 5.0. The super-quadric major axis length is distributed between 0.8 and 1.6 mm, and the super-quadric aspect ratios b/a and c/a between 0.8 and 1.0. The bulk material density is 1600 kg/m^3 . The spring stiffness k of 600 N/m was chosen to maintain average particle overlaps to be smaller than 0.5% of the particle radius. The coefficient of restitution e was chosen as 0.75, and the coefficient of friction μ as 0.70 from simple experiments. The container object is a cylinder with inner radius of 37.5 mm and length of 200 mm. A 20% fill level corresponds to 50105 particles.

The objective for the simulation presented here is to study the particle motion where the kinematics of the cylinder are fully specified using container velocities directly measured in the experiment (Dragomir et.al. 2008). The motion of the container is characterised from a high-speed video of the experiment. The derived horizontal and vertical velocities, and the spin of the container are then specified at 20 ms intervals for the simulation.

A comparison of the imposed container locations during the simulation (above) and experiment (below) is given in Figure 2. The images are shown with 160 ms intervals until the motion ceases at 900 ms after the instant of release. Particles are colored by their speed, with blue representing 0 m/s and red 1.5 m/s.

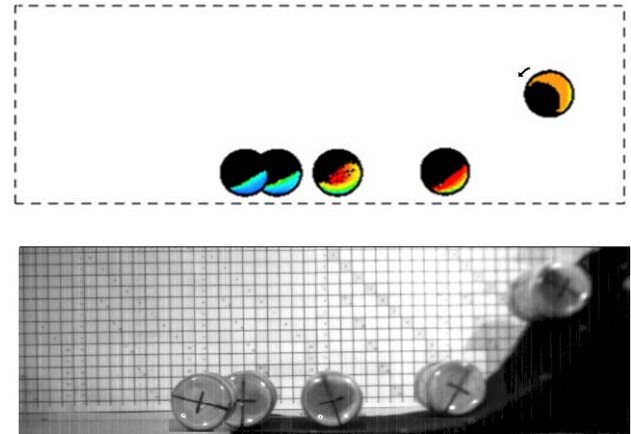


Figure 2: Sample container locations for the simulation (above) and experiment (below) at 160-ms intervals. Simulation particles colored by speed from stationary (blue) to 1.5 m/s (red).

Numerical Predictions

In Figure 3, close-up views of the container are presented to show the details of the granular flow field. The images are presented at different times, to highlight specific flow events related to the particle and container motion. Numerical and experimental images are shown in in

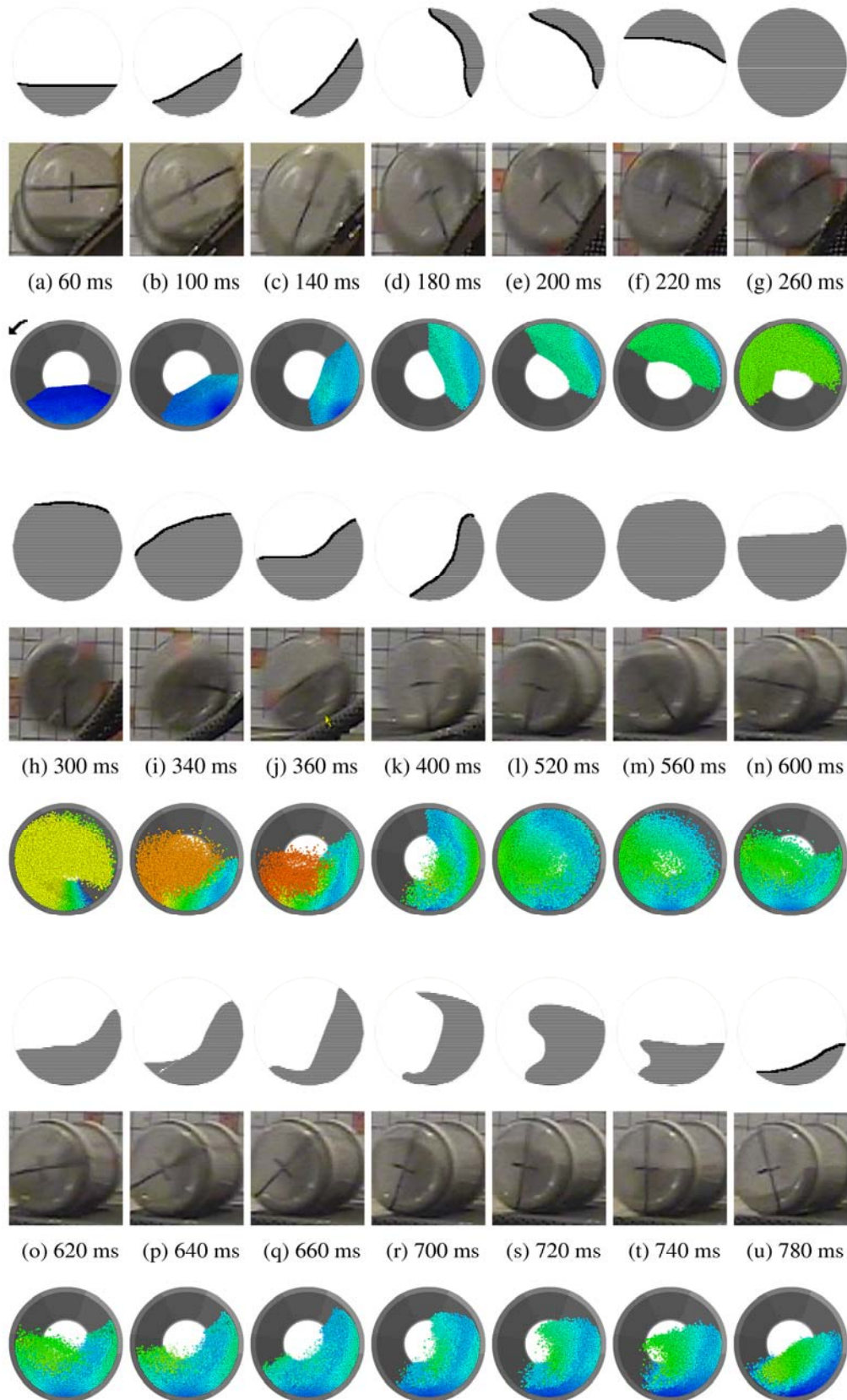


Figure 3: Comparison of experimental and numerically predicted surface shapes. The first row of each group is a schematic illustration of the second row, photographs from the experiment, followed by DEM predictions. Particles from simulation are colored on the same scale as in Figure 1. The arrow represents the direction of rotation.

conjunction with schematic illustrations of the particle distribution in the container. Schematic illustrations are in the first row of each group, experiments given in the second rows, and the numerical predictions in the third rows. For the simulation data, an isometric view of the container is given from the front wall where the white circular area in the center of the container represents the back wall.

Three significant flow events are observed. Firstly, two centrifuging events occur where the particles can be seen lining the container wall and which then collapse under gravity. A third event is observed as a cataracting stream where some particles become airborne but have insufficient energy to centrifuge. The particles finally come to rest soon after the container reaches the horizontal plane. These three events are discussed next in more detail.

For the first 200 ms, particles move as a rigid body, as shown in Figure 3 (a-e). From 200 to 300 ms, the particles centrifuge and line the container walls as it accelerates down the ramp as seen in Figure 3 (f-h). Particles near the top of the container collapse under gravity falling to the bottom of the container between 300 ms and 360 ms as shown in Figure 3 (h-j). The experiment and simulation show nearly identical particle motions for these frames. In the simulation, at 300 ms the majority of the particles have a speed of 1.2 m/s. By 340 ms, the remaining airborne particles have increased their speed to 1.4 m/s, while those in contact with the wall average 0.7 m/s.

The particles centrifuge for the second time between 520 and 600 ms just as the container reaches the flat surface. Matching particle bed surface shape in the container for the numerical and experimental observations can be observed between 600 and 620 ms, in Figure 3 (n-o). Particle speeds are slower than the previous centrifuge, with average speeds being only 0.8 m/s for both the container wall and the airborne particles.

From 700 ms, Figure 3 (r-w), a single cataracting stream is observed in both the experiment and the simulation. The airborne particles approach 0.7 m/s, while the container wall particles travel at 0.2 m/s for this event. Particle motion ceases completely at 900 ms.

For all three events discussed, free surface shapes from experimental observations and numerical predictions match closely. With this confidence in the flow predictions, the dissipation mechanisms predicted by DEM are discussed next.

The total, instantaneous dissipation power plotted against time is shown in Figure 4. The three events discussed in relation to Figure 3 earlier, are marked in this figure. The first event is centered around the first centrifuging event particle collapse, with peak dissipation at 340ms (see Figure 3 (i)). The second event is much smaller in magnitude and peaks at 540 ms (see Figure 3 (l-m)). The third event occurs after the cataracting stream collides with the container wall, at 790 ms (see Figure 3 (u)).

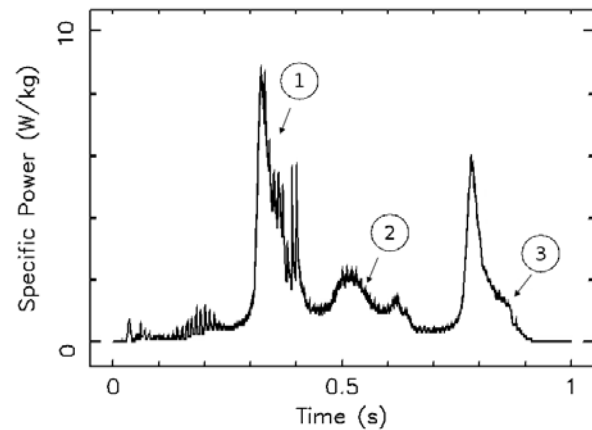


Figure 4: History of instantaneous dissipation power.

Each collision can be disaggregated into forces. The normal component for the dissipation is due to the dashpot (viscous damping force) $C_n V_n$. The tangential dissipation component $C_t V_t$ is responsible for frictional losses. The energy dissipated in these dashpots defines the instantaneous dissipation power, shown in Figure 4.

The normal and tangential components of energy dissipation are shown in Figure 5. Four snapshots are shown between 340 ms and 400 ms, which indicate the localized energy dissipation. The particles are colored according to the sliding scale shown on the right. The scale for the shear dissipation is twice that for the normal dissipation.

The first large peak around 340ms in Figure 5 corresponds to the collapse of particles after centrifuging. As a result, the top layer of the particle bed experiences collisions at large speeds with airborne particles. Significant amounts of energy are also dissipated through shear in the center of the particle bed as shown in Figures 5 (a) and 5 (b).

The energy dissipation during the second centrifuge and collapse of the particles between 500ms and 600ms, is given in Figure 6 in the same format as Figure 5. While there are many airborne particles, only a small number of the total particles are involved in high dissipative losses. Also airborne particle speeds are slower than the first centrifuge/collapse, thus both total and peak energy dissipation is rather poor.

The difference between the first and second events regarding energy dissipation is intriguing. The magnitude of the dissipation is much larger in the first than in the second event. A likely explanation is that particles for the first event become airborne near the top of the ramp, then free-fall over a larger vertical distance to strike the bed surface than the particles for the second event, which collapse under gravity from the top of the cylinder. This is supported by Figure 3 (h-j) and (k-n), since the airborne particles in the first event have much higher average speeds than those in the second event.

Particles coloured by normal and tangential energy dissipation rate for the third event are shown in Figure 7, the cataracting stream of particles between 760ms and 820ms. Although the absolute speeds of the cataracting particles are relatively small, 0.1m/s, there are steep velocity gradients which cause significant shear at the trailing end (far left end) of the bed. It is also noticeable that there is considerable normal dissipation around the same trailing end of the bed due to the cataracting particle stream and the avalanching surface layer impacting at the wall. It is worth noting that while the

airborne speeds of the cataracting particles in event 3 are much smaller than those in event 1, comparable levels of energy dissipation are observed in Figure 5. This suggests that shear dissipation from the avalanching surface layer (rather than impacts from cataracting particles) is the dominant energy loss mechanism controlling the stopping distance of the container. Maintaining a steady avalanching regime through control of the container's angular speed could conceivably provide a controlled level of shear dissipation which would be a desirable property for a granular absorber.

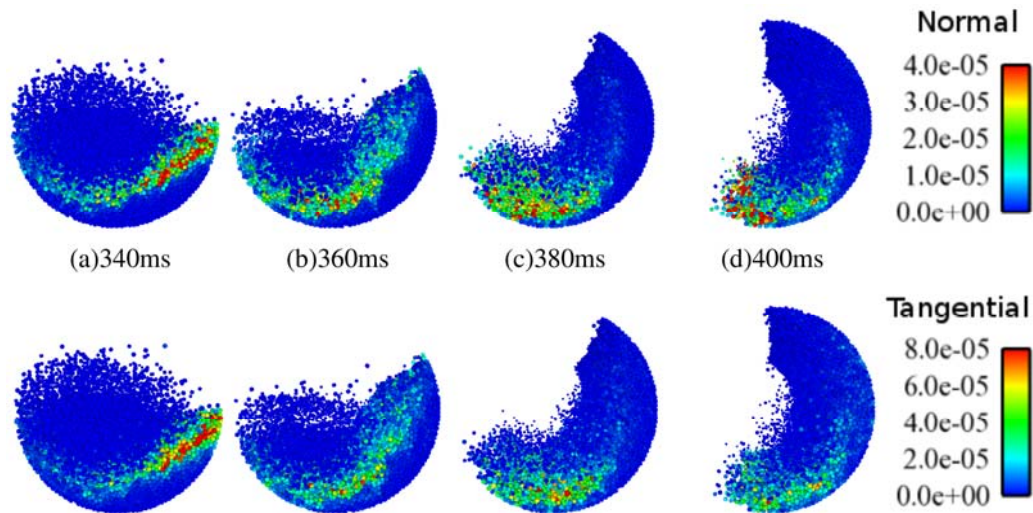


Figure 5: Energy dissipation for the first event in Figure 4. Top row is for the normal direction, and the bottom row for the tangential direction.

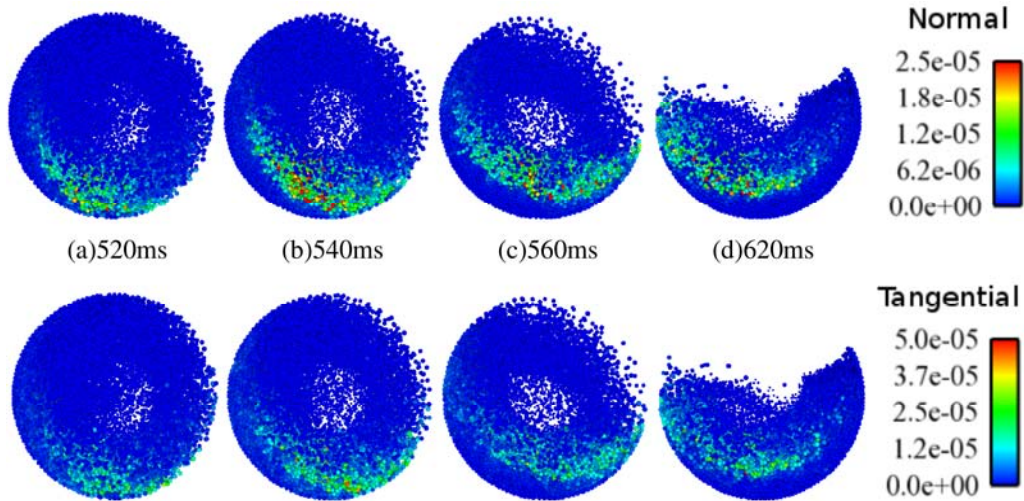


Figure 6: Energy dissipation for the second event in Figure 4.

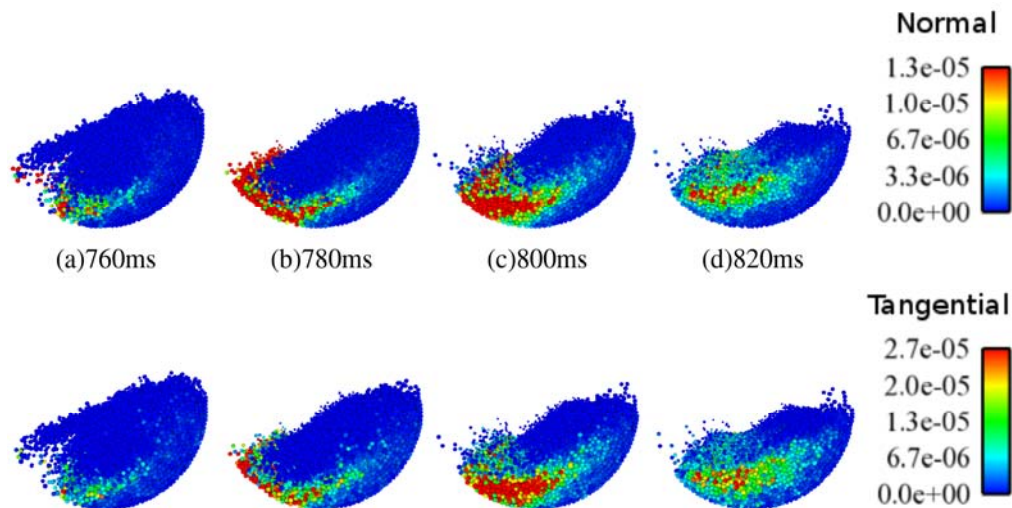


Figure 7: Energy dissipation for the second event in Figure 4.

In summary, the numerical predictions obtained with the DEM solver closely match the experimentally observed particle motion. Hence, further analysis of the numerical simulations can be used to draw more in-depth conclusions on the nature of the energy dissipation. Such details are not possible to obtain from the experiments alone.

CONCLUSION

A numerical prediction model of the particle flow in a rotating drum was presented. Kinematic comparisons of the particle flow between the simulation and the experiment show a good match, when the container motion is imposed using data from the experiment. The particle flow consisted of three distinct events, which are also characterised in the energy dissipation of the system. These comprise of the collapse of a centrifuging particle stream when the system has significant energy and a cataracting stream prior to system coming to rest. Energy dissipation characteristics of the system derived from the simulation were discussed. Two energy dissipation mechanisms were found: the collisions at the particle bed surface during the cataracting stream collapse, and shear layers when the particles flow in a avalanching regime. Shear through tangential components of collisions was found to be the primary energy dissipation method, accounting for two thirds of the total. We assert that for a feasible structural damper design control over the particle flow regime is essential, as it would provide both predictability and optimal performance. Further study of the energy dissipation in rotating drums partially filled with a granular material is currently under way, in the form of a fully dynamic model.

REFERENCES

- DRAGOMIR, S. C, SEMERCIGIL, E. S, TURAN, O. F., (2007) "Induced Particle Sloshing In A Rotating Container, 16TH Australasian Fluid Mechanics Conference, 1207-1212.
- DRAGOMIR, S. C, SINNOTT, M., SEMERCIGIL, E. S, TURAN, O. F., (submitted 2009), "Energy Dissipation Characteristics of Particle Sloshing in a Rotating Cylinder", *Journal of Sound and Vibration*.
- CAMPBELL, C. S., (2006), "Granular material flows - An overview", *Powder Technology*, **162**, 208-229.
- BARKER, C. G., (1994), "Computer simulations of granular materials", in: *Granular Matter, A. Interdisciplinary approach*, Ed. A. Mehta, Springer-Verlag, NY, 35-84.
- WALTON, O. R., (1992), "Numerical simulation of inelastic frictional particle-particle interaction", in: *Particulate two-phase flow*, Ed. M. C. Roco, Butterworth-Heinemann, 884-911.
- CLEARY, P. W., (1998), "Predicting charge motion, power draw, segregation, wear and particle breakage in ball mills using discrete element methods", *Minerals Engineering*, **11**, 1061-1080.
- CLEARY, P. W., (2001), "Recent advances in DEM modelling in tumbling mills", *Minerals Engineering*, **14**, 1295-1319.
- SINNOTT, M, CLEARY, P. W., and MORRISON, R., (2006), "Analysis of stirred mill performance using DEM simulation: Part 1 - Media motion, energy consumption and collisional environment", *Minerals Engineering*, **19**, 1537-1550.
- CLEARY, P. W., (2008), "The effect of particle shape on simple shear flows", *Powder Technology*, **179**, 144-163.
- CLEARY, P. W., and SINNOTT, M. D., (2008), "Assessing mixing characteristics of particle-mixing and granulation devices", *Particuology*, **6**, 419-444